2017 IEEE International Conference on Robotics and Automation (ICRA)
Singapore, May 29 - June 3, 2017

Fabric Sensory Sleeves for Soft Robot State Estimation

Michelle C. Yuen[1], Henry Tonoyan[2], Edward L. White[1], Maria Telleria[2] and Rebecca K. Kramer[1]

***Abstract*— In this paper, we describe the fabrication and testing of a stretchable fabric sleeve with embedded elastic strain sensors for state reconstruction of a soft robotic joint. The strain sensors are capacitive and composed of graphite-based conductive composite electrodes and a silicone elastomer dielectric. The sensors are screenprinted directly into the fabric sleeve, which contrasts the approach of pre-fabricating sensors and subsequently attaching them to a host. We demonstrate the capabilities of the sensor-embedded fabric sleeve by determining the joint angle and end effector position of a soft pneumatic joint with similar accuracy to a traditional IMU. Furthermore, we show that the sensory sleeve is capable of capturing more complex material states, such as fabric buckling and non-constant curvatures along linkages and joints.**

Keywords: soft material robotics, hydraulic/pneumatic actuators, flexible robots

I. Introduction

Pneumatically-actuated robotic systems have the potential to fill gaps left open by traditional rigid robots. The materials comprising pneumatic actuation systems, such as fabrics and elastomers, are lightweight and flexible. As a result, pneumatic systems are inherently soft, well-suited for operation alongside similarly soft humans, and easily compacted for efficient packing and transport. Because of their ability to withstand much larger deformations and intrinsic damping properties, pneumatic robots are robust to large impacts and are able to adapt to complex, poorly-defined environments. These are significant challenges for rigid robotic manipulators because interaction with their surroundings requires that the manipulator either actively or passively match its compliance to each physical interaction [1].

While there has been a great deal of work on the design and open-loop control of pneumatic actuators, proprioceptive feedback onboard the pneumatic systems has seen limited development [2] [3]. The compliance of a pneumatically-driven system makes it inherently under-actuated (*i.e.,* the system has more degrees of freedom (DoF) than it has control over). As a result, it is a challenge to identify the state of the system for closed-loop control of pneumatically-driven robots.

To address this challenge, highly deformable soft robotic systems require equally deformable sensors for state estimation. Recent work in the area of high-deformation elastomer-based strain sensors has shown that they are capable of measuring the large strains that occur on the surface of pneumatic actuators. In this paper, we bring together soft sensing with pneumatic actuation to perform joint angle proprioception. We embedded silicone elastomer-based sensors into Spandex fabric to form a sensory sleeve, which was secured around a pneumatic joint. The test platform used in this paper, henceforth referred to as the Grub, was developed by Otherlab Pneubotics. It is a single DoF robotic arm composed of two passive linkages on either side of an antagonistic pneumatic actuator pair. Constructed of high-strength fabrics, the Grub is capable of lifting eight times its own weight. The sensory sleeve wraps around the bellows of the Grub to measure the change in longitudinal length of the bellows as they are inflated and deflated to cause joint flexion and extension (Figure 1). By fabricating the sensors onto removable sleeves, we were able to balance ease of iterative design by testing different sensor layouts on the Grub with progress towards a large-scale manufacturing process, which reduces the complexity and cost of incorporating sensing into the structure of the robotic platform.

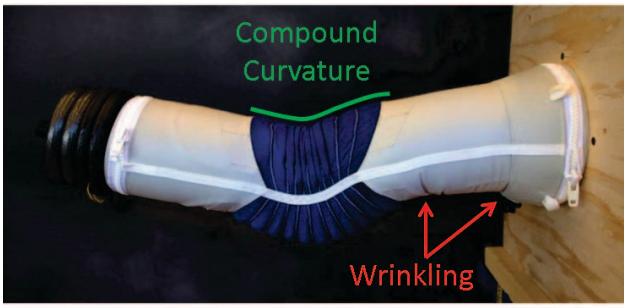

Fig. 1. Grub joint as it flexes to lift 15lbs. Wrinkling is observed in the fabric near the base of the Grub, resulting in buckling of the linkage and causing unintended vertical deflection of the end effector. Compound curvature is observed along the length of the actuation bellows.

The contributions of this work are: 1) manufacture of a sensory array into a stretchable fabric, 2) demonstration of a sensor-embedded fabric sleeve in reconstructing the joint angle of a pneumatically-actuated joint, the results of which are verified through comparison of this sensory sleeve to inertial measurement unit (IMU) and motion capture measurements of joint state, and 3) application of discrete sensors towards detecting smaller-scale and more complex system states, such as buckling in passive links.

II. Previous Work

Soft strain sensors, particularly for strains greater than 50%, can be divided into two categories: resistive and capacitive. Resistive strain sensing transduces strain into

[1]MCY, ELW, and RKK are with the School of Mechanical Engineering, Purdue University, West Lafayette, IN, USA. [2]HT and MT are with Otherlab Pneubotics, San Francisco, CA, USA. email: {yuenm, white335, rebeccakramer}@purdue.edu; {henry, maria}@otherlab.com

a change in resistance. In one approach, microchannels containing a conductive fluid such as a liquid metal or ionic liquid are embedded into elastomer materials [4] [5] [6]. Strain applied to the material causes a change in length and cross-sectional area of the conductive fluid, resulting in a change in resistance. Another approach to a resistive strain sensor uses conductive silicone elastomer composites. In these devices, conductive particles such as graphite [7], carbon nanotubes [8], and silver nanowire [9], are dispersed within a silicone elastomer matrix. As strain is applied to the material, the particles decrease contact with one another, resulting in a higher resistance. Yet another approach to resistive strain sensing uses conductive yarns and fabrics. The fibers comprising the yarn or fabric are made of conductive material, such as stainless steel thread, or are coated in conductive particles [10] [11]. As strain is applied, the conductive fibers comprising the yarn increase contact with one another, decreasing the resistance of the yarn.

Capacitive strain sensing transduces strain into a change in capacitance. These sensors are composed of parallel electrodes separated by a dielectric layer. Merritt *et al.* used sliding electrode plates to convert changes in chest diameter during respiration to a change in capacitance [12]. Alternatively, researchers have made capacitive sensors that use a parallel-plate electrode construction that rely upon the Poisson effect in the dielectric material. As the sensors are stretched, the electrode area increases and the dielectric thickness decreases, resulting in an increase in capacitance. The stretchable electrode layers have been made using thin metal films [13], or more commonly, silicone embedded with carbon nanotubes [14] [15], carbon black [16] [17], or silver nanowires [18]. Researchers have demonstrated the application of discrete elastomer-based capacitive strain sensors towards capturing human motion [17] [18] and microrobotic linkage displacement [15].

Various researchers have demonstrated control of a 1DoF pneumatically actuated joint using IMU data to capture joint angle. Best, *et al.* determined the efficacy of using model predictive control and a single pressure input to control the joint angle of a predecessor to the Grub used in this work [19]. Gillespie *et al.* demonstrated the ability to simultaneously control the stiffness and the angle of the Grub joint [20]. Both [19] and [20] relied upon IMUs placed on the linkage furthest away from the fixed base to capture joint angle data. However, IMUs are susceptible to drift over time, requiring frequent re-calibration [21]. Additionally, the use of IMUs to measure joint angle implies that the linkages are treated as rigid elements, whereas, in our system, they are susceptible to buckling and drooping, as seen in Figure 1. As the number of soft joints and linkages in series increases, these small errors from drift and passive linkage displacement will add up to large errors when estimating the location of the end effector.

Other approaches to state estimation of a pneumatic actuator have used visual feedback. Marchese, *et al.* relied upon the use of multiple external cameras [22], whereas Wang *et al.* performed visual servoing by affixing a camera to the end of the robotic arm to track the position of the end effector relative to a fixed point on a reference frame [23]. Although visual-based proprioception has been demonstrated in a controlled setting, it is limited by the infrastructure required to hold cameras or reference frames in place. In contrast, a sensory sleeve integrated into the structure of the pneumatic joint allows the system to operate more freely, as it does not require additional environmental infrastructure.

The application of soft sensing devices to proprioception and potential closed-loop control of soft inflatable robotic structures remains an emerging field of research. Park, *et al.* demonstrated the use of embedded liquid metal strain gauges to detect the state of a McKibben actuator [24]. This work was extended towards an all-elastomer sleeve with distributed modules of penumatic actuators with embedded sensing [25]. Farrow, *et al.* and Bilodeau, *et al.* demonstrated integration of liquid metal-based sensors directly into a pneumatic gripper [26] [27]. The structures of these devices are composed primarily of elastomers, easing the integration of elastomer-based sensing devices. In contrast, the Grub penumatic joint is composed of fabrics. We therefore focused our integration approach on compatibility with fabric substrates, which lends well to both fabric-based soft robots and wearable sensory garments.

III. Hardware

A. Sensor-embedded Sleeve

The sensors embedded in the sleeve are flexible and stretchable parallel-plate capacitors that consist of a dielectric layer sandwiched between two conductive electrode layers. The electrode layers are a conductive composite made up of silicone elastomer (DragonSkin10, Smooth-On Inc.) and expanded intercalated graphite (10wt%). During fabrication of the sensors, the conductive composite is processed with 2.36wt% graphite, 21.26wt% silicone elastomer, and 76.38wt% cyclohexane to ensure homogeneous dispersion of graphite within the silicone elastomer. Cyclohexane is a volatile organic solvent that does not affect the final properties of the silicone elastomer nor the conductive composite once it vaporizes and the elastomer cures. The dielectric material is composed of a mixture of 4 parts DragonSkin 10 Slow and 1 part Silicone Thinner (Smooth-On Inc.). The fabric is stretchable Lycra material (Payless Fabrics).

The sensory sleeve is fabricated using a screenprinting technique. The schematics for the sensors are shown in Figure 2(a,b). Masks for each layer are made by laser-cutting the pattern out of polyethylene terephthalate (PET) film. The fabric is secured with tape to a flat surface. First, a base layer composed of the dielectric material is screenprinted onto the fabric by scraping a threaded rod across the surface. Once the base layer is cured, the mask for the bottom electrode layer is aligned over the base layer. The bottom electrode is then screenprinted over the base layer and the mask is immediately removed to prevent the electrode material from wicking under the mask and spreading over the base layer. After the bottom electrode cures, the dielectric layer and top electrode layers are screenprinted in the same manner as

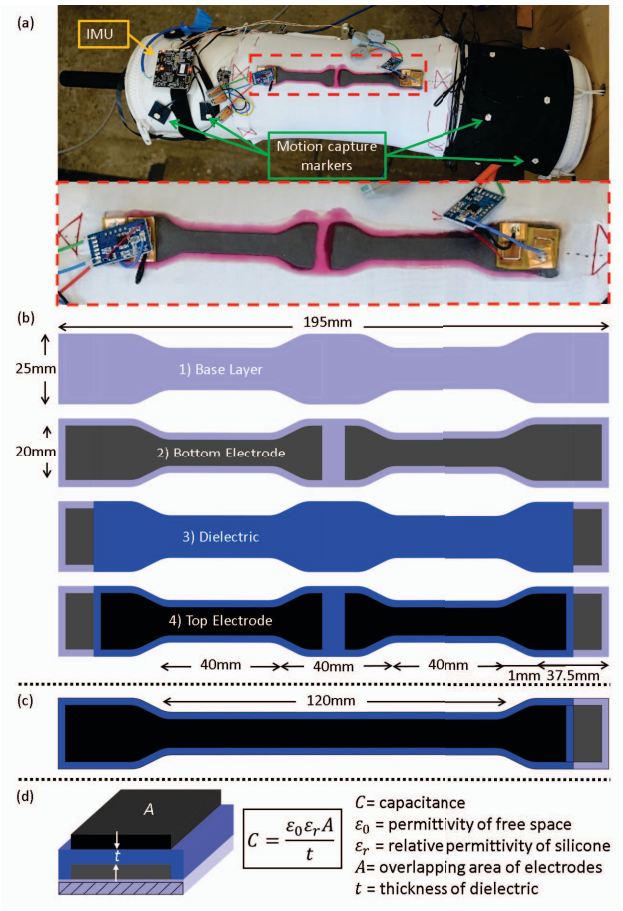

Fig. 2. (a) Top-down view of the dual-sensor sleeve wrapped around the Grub and a zoomed in view of the sensors, copper interface and signal conditioning boards. The dual-sensor pair is mirrored on the bottom of the Grub. (b) Schematic of the screenprinted layers for dual-sensor designs, shown in the order they are patterned in, from top to bottom. (c) Schematic of the screenprinted single-sensor design. (d) Schematic of the cross-section of a sensor and the relationship between the sensor's capacitance and the geometry of the layers.

the bottom electrode. The dielectric layer is designed with a 2.5mm margin offset outward from the bottom electrode to prevent the top electrode from wicking down the edge of the sensor and contacting the bottom electrode. For interfacing, the bottom electrode is not fully covered by the dielectric layer at one of the ends of the sensor, leaving a 10mm long portion exposed for interfacing. Looking at the cross-section of the sensors, the approximate thicknesses of the elastomer-infiltrated fabric base, bottom electrode, dielectric layer, and top electrode are 500, 150, 300, and 150μm, respectively.

Copper-clad polyimide sheets (Pyralux, Adafruit Industries) were sewn onto the end of the sensor, making contact with both the top and bottom electrode layers. In order to prevent the thread from electrically bridging layers at the sew holes, a coring punch (1.75mm, Harris UniCore) was used to punch out holes in the sensor before sewing. Wires were then soldered to the copper, linking the sensor to the signal conditioning board.

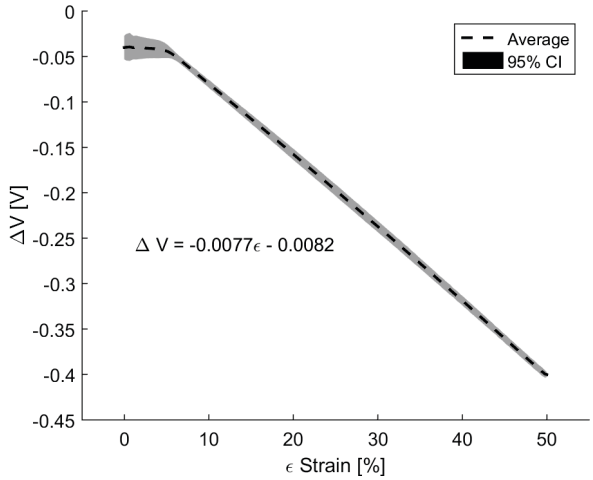

Fig. 3. Response of screenprinted sensors due to applied displacement causing strains from 0-50% for 20 cycles. The average and confidence interval is taken from data for 3 individual sensors. ΔV is calculated as $\Delta V = V - V_0$, where V is the sensor output and V_0 is the initial sensor reading.

B. Signal Conditioning Board

The signal conditioning board transduces the change in capacitance of the sensors to an analog voltage. The boards were custom-designed to minimize the amount of rigid materials used in the sensory sleeve. To measure the capacitance, each board charges up the capacitive sensor to 2.262V and measures the time it takes to discharge back to 0.238V. The frequency at which the charging occurs is tuned to match the time constant of the capacitive sensor. Changing the charging frequency allows us to tune the sensitivity of the signal conditioning board. For the sensors on the joint, the charging and discharging cycle period is 8.4ms. The analog voltage output is linearly related to the capacitance.

C. Pneumatic Arm

The Grub is a pneumatic arm composed of two passive linkages on either end of an active 1DoF joint. The passive linkages are composed of air bladders inside of reinforcing PVC fabric cylindrical shells. The passive linkages are pressurized to approximately 10psi throughout operation. The active joint consists of two antagonistic bellows-like bladders reinforced by ballistic nylon. Inflation of these bellows is controlled by valves regulating the flow of compressed air. Changing the pressure differential between antagonistic bellows causes the change in joint angle.

IV. Characterization and Modeling

A. Sensor Characterization

The sensors were characterized individually to determine their response to linear extension. As the sensor is stretched, the area of the electrodes increases while the thickness of the dielectric layer decreases, causing a change in capacitance that is transduced to a change in voltage (Figure 2(d)). The voltage output is linear with respect to applied displacement,

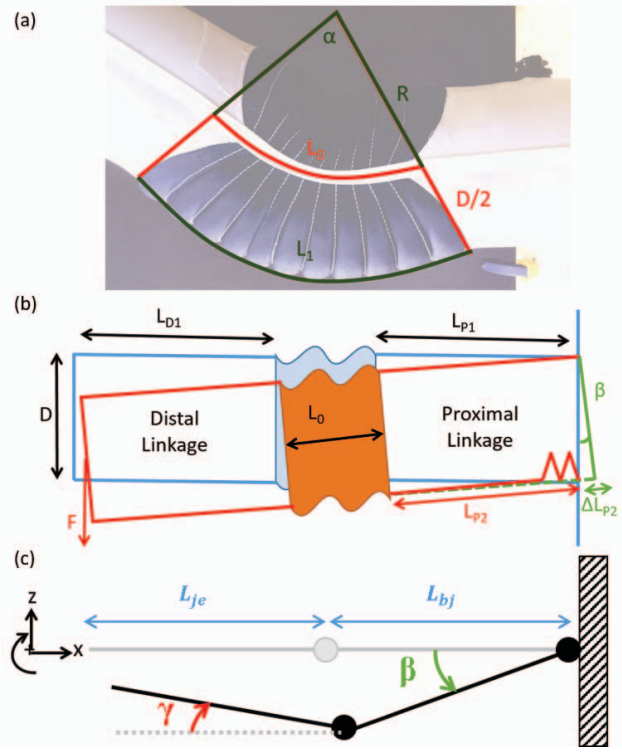

Fig. 4. (a) Schematic showing the relationship between joint curvature and sensor length. (b) Schematic showing buckling of the proximal linkage near the base. (c) Schematic combining proximal joint buckling with actuation.

with no discernible cycle-to-cycle hysteresis (Figure 3). However, this linear trend breaks down at low strains (<5%), due to the polymer-based Spandex fabric plastically deforming and therefore causing the sensor to be slack at low strains. This "break-in" length is typical of a polymer system (stress relaxation) and can be accommodated by pre-straining the sensor beyond what it will encounter in operation.

B. Grub Modeling

We generated models of the Grub's geometry for constant curvature joint flexion and for combined joint flexion and linkage buckling. As the bellows on one side of the joint are inflated, the arc length along the outside of the joint, L_1, will increase linearly with respect to the joint angle, α (Figure 4(a)):

$$(R+\frac{D}{2})\alpha = L_1 = L_0 + \Delta L \tag{1}$$

where R is the radius of curvature to the midline of the Grub, D is the diameter of the Grub, L_0 is the length of the midline seam, L_1 is the length along the outside of the joint, and ΔL is the change in length from L_0 to L_1.

Using the characterization of the sensors (Figure 3), the change in length of a sensor placed along the outside of the joint, ΔL, can be calculated as a function of the sensor output:

$$\Delta L = C_1 \cdot \Delta V \tag{2}$$

where C_1 is the slope of the linear regression of the sensor characterization and ΔV is the change in voltage output of the sensor.

Substituting ΔL into Eq. 1, the joint angle can be calculated as a function of the sensor output:

$$\alpha = \frac{L_0 + C_1 \cdot \Delta V}{R + \frac{D}{2}} \tag{3}$$

We note here that changing the boundary conditions during sensor extension changes the sensor response. For example, the response of the sensor extended in free space differs from the response of the sensor extended across the joint [28]. This is due to the addition of the surface normal force that arises as the joint bellows are inflated, which compresses the dielectric layer more than when applying axial strain in free space. However, the sensors response is linear regardless of boundary conditions, and calibration in a specific operating condition will yield the value of C_1 in Eqs. 2 and 3.

When the Grub is lifting larger payloads, wrinkling in the fabric of the proximal linkage will cause buckling near the base (Figure 4(b)). The base angle, β, is the angle between the proximal linkage and horizontal:

$$\beta = sin^{-1}\left(\frac{\Delta L_{P2}}{D}\right) \tag{4}$$

where L_{P2} is the contracted length of the bottom of the proximal linkage due to buckling, and ΔL_{P2} is the difference between the nominal length of the proximal linkage L_{P1} and the contracted length L_{P2}. As a result of this buckling, the vertical and horizontal displacements of the end effector, Δz and Δx, are a function of the base angle β and the distal linkage angle γ:

$$\Delta z = (L_0 + L_{P1} + L_{D1})sin\beta + L_{je}sin\gamma \tag{5a}$$

$$\Delta x = (L_0 + L_{P1} + L_{D1})(1 - cos\beta) + L_{je}(1 - cos\gamma) \tag{5b}$$

where L_{D1} is the nominal length of the distal linkage, γ is the angle of the distal linkage relative to horizontal and L_{je} is the length between the joint center and the end effector. We also note the length between the joint center and the base, L_{bj}, as shown in Figure 4(c). Depending on the loading condition, the joint center may be located anywhere along the joint midline seam L_0.

V. State Reconstruction

We first calibrated the sensors *in situ* and then performed a test for state reconstruction. In particular, we were interested in capturing the joint angle and the end-effector position of the Grub. The test platform was composed of a Grub positioned horizontally with 1) single sensors on the top and bottom of the joint to measure joint angle, 2) a sensor laid along the bottom of the proximal linkage to measure buckling, 3) an IMU placed on the top of the distal linkage near the end effector, and 4) two sets of LED motion capture markers wrapped around each of the proximal and distal linkages (Figure 2(a)). The voltage signals from the sensors were captured using the controller unit that also housed the IMU. The motion capture data served as the ground truth data, which we used to both calibrate the system and quantify the accuracy of other measurement methods.

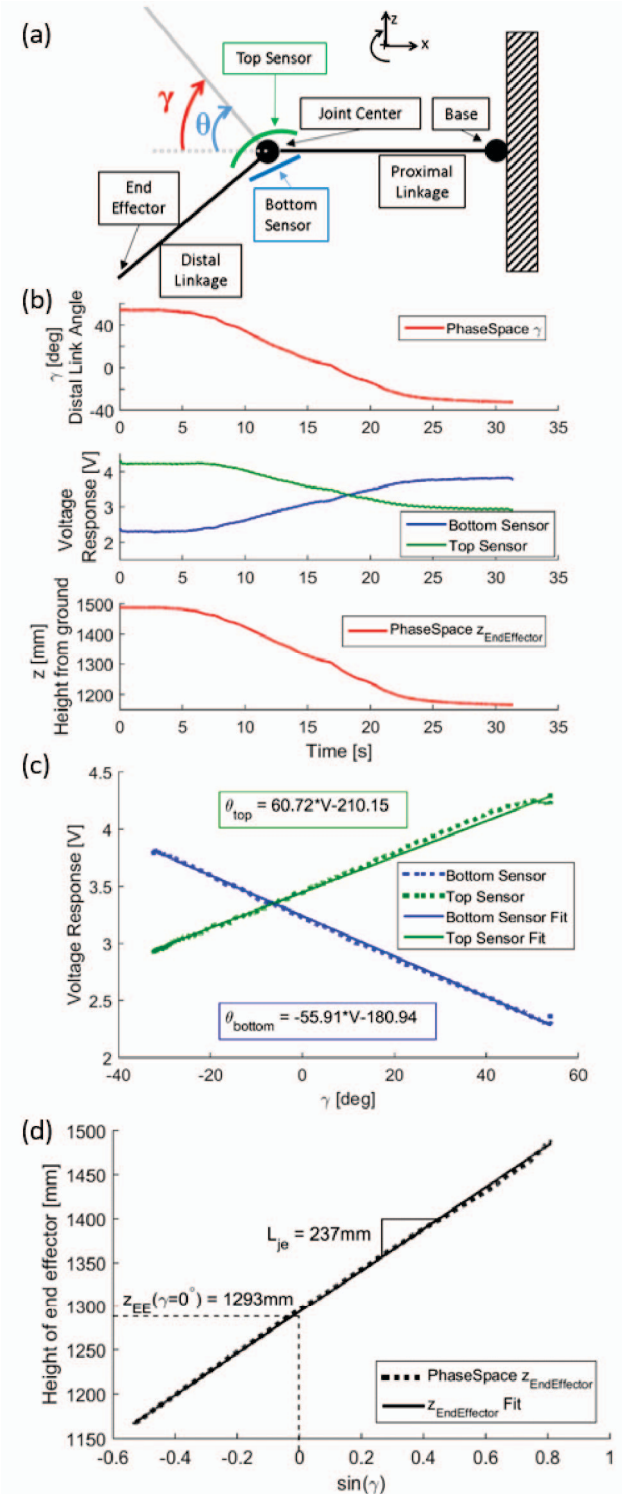

Fig. 5. First calibration phase for measuring the joint sensor response as a function of joint angle and determining the effective length of the distal linkage. (a) Experimental procedure where the Grub is swept from the light gray trace to the black trace. (b) Data from the PhaseSpace motion capture system and strain sensors while sweeping the Grub distal linkage downwards. (c) Plot of the measured joint angle, θ, vs. the voltage response of the sensors. The linear regression equations are listed. (d) Vertical position of the end effector as a function of the angle of the distal linkage. The slope of this linear regression is the effective length between the apparent joint center and the end effector. For both plots, the dashed line indicates raw data and the solid line indicates a linear regression.

The experimental procedure consisted of two calibration phases followed by a validation phase. The two calibration phases were performed to determine the strain sensors' responses on the Grub in operation and to identify the effective joint center and linkage lengths. The center of rotation of the joint can change under different loading conditions and is not easily identified. By performing these two calibration steps, the vertical displacement and the angle of the joint can be calculated using solely the sensor array on the surface of the Grub. To validate this, we compared the state reconstruction from sensor array data to IMU data and the ground truth generated with the motion capture system (PhaseSpace Systems).

A. Joint Angle Calibration

The first calibration phase was performed to determine the strain sensors' voltage response to joint angle and to identify the effective length of the distal linkage (*i.e.* the length between the apparent joint center and the end effector). Because the response of the sensors on the Grub differs from the response when pulling the sensors in free space, we calibrated the sensors on the Grub. In order to generate this data, the Grub was actuated in an unloaded state so that a constant curvature bend was achieved throughout the range of motion and the proximal linkage stayed parallel to the ground (Figure 5(a)). In this test, the angle β from Figure 4(c) is 0°, and therefore, the angle of the distal linkage with respect to the ground, γ, is equal to the joint angle θ. The data from the PhaseSpace motion capture system, IMU and strain sensors are shown in Figure 5(b). Using this data, we extracted the angle $\gamma = \theta$ and used it to calibrate the sensors on the joint. The results, shown in Figure 5(c), demonstrate that the sensors indeed have a linear response with respect to joint angle. The regression equations for the top and bottom sensors are shown on the plot and are used for the second calibration phase to find the joint angle θ when the Grub is loaded.

In addition to finding the relationship between the sensor response and the joint angle, we determined the effective location of the center of the joint relative to the end effector. This information yields the apparent length of the distal linkage, L_{je}, which is composed of the entire length of the passive distal linkage and part of the length of the bellows. To find L_{je}, we constructed a right triangle with L_{je} as the hypotenuse and $z - z_{EE}(\gamma = 0^\circ)$ as the leg opposite γ, where z is the height of the end effector and $z_{EE}(\gamma = 0^\circ)$ is height of the end effector when both linkages are horizontal (Figure 5(a)). Using $z = L_{je} * sin(\gamma)$, we found the slope of the linear regression in Figure 5(d) to determine L_{je}.

B. Base Angle Calibration

The second calibration phase simulated a buckling event wherein the fabric on the bottom of the proximal linkage near the base wrinkles inward, causing the entire pneumatic arm to bend downwards. We determined the response of the buckling sensor, which was fastened along the bottom of the proximal linkage, to the change in angle of the proximal

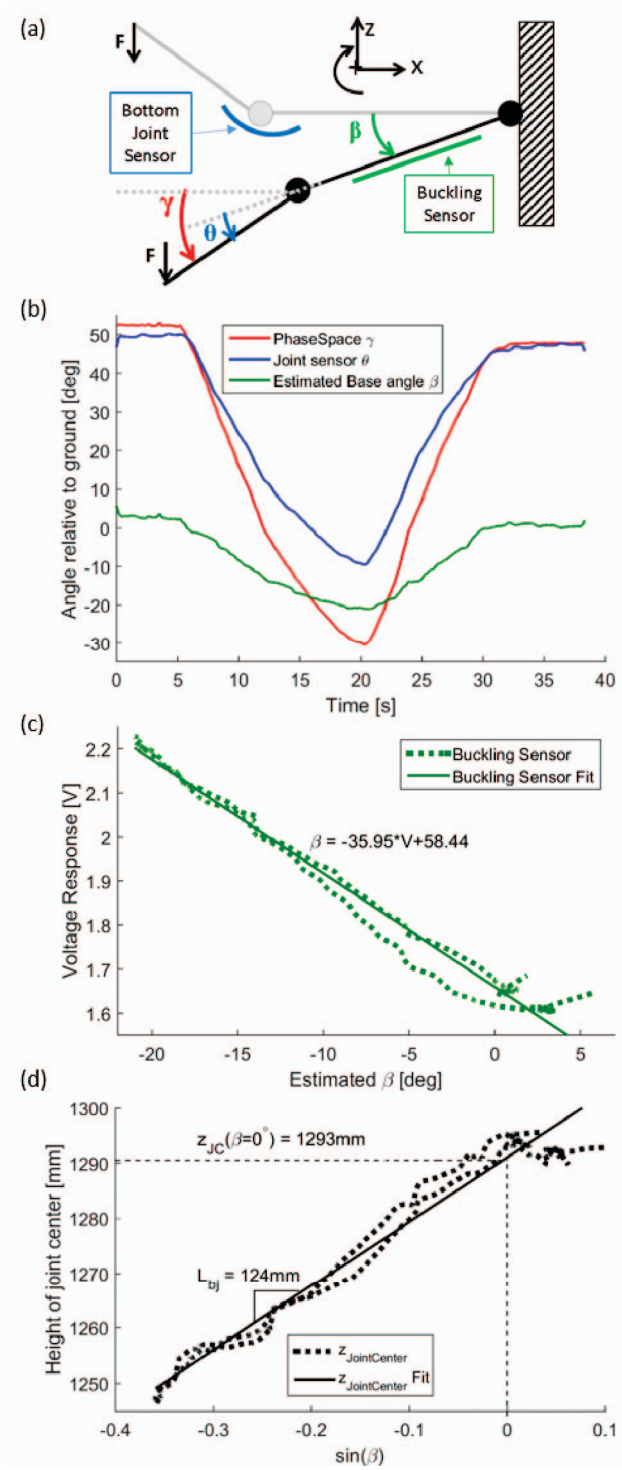

Fig. 6. Second calibration phase for measuring the buckling sensor's response to linkage buckling near the base and determining the effective length of the proximal linkage. (a) Experimental procedure where the Grub is forced downward from the light gray trace to the black trace. (b) Data from the PhaseSpace motion capture system and joint angle strain sensors while forcing the Grub distal linkage downwards and causing buckling to occur near the base. The estimated base angle, β is the difference between γ and θ. (c) Plot of β vs. the voltage response of the buckling sensor. The linear regression equation is listed. (d) Plot of the vertical position of the joint center vs. $\sin(\beta)$. The slope of this linear regression is the effective length between the apparent joint center and the base. The height of the joint center when no buckling at the base occurs is marked. For both plots, the dashed line indicates raw data and the solid line indicates a linear regression.

linkage due to buckling near the base. We also identified the effective length of the proximal linkage (*i.e.* the length between the base and the apparent joint center). After relating the joint sensor outputs to the joint angle, we performed a base angle calibration. To do this, we first actuated the unloaded Grub to an upright position ($\theta \approx 50^{\circ}$) and then manually forced the end effector downwards, extending the joint and forcing the proximal linkage to buckle near the base (Figure 6(a)). The motion capture system was used to capture γ while the bottom joint sensor and buckling sensor responses were recorded (Figure 6(b)). Using solely the bottom joint sensor, we determined the joint angle θ using the corresponding calibration equation shown in Figure 5(c). Using the relationship $\beta = \gamma - \theta$, we determined β, the angle of the proximal linkage due to buckling near the base. We then plotted the response from the buckling sensor against the estimated base angle and fit a line to determine the buckling sensor's response with respect to β (Figure 6(c)). We also determined the base-to-joint length, L_{bj}, by finding the slope to the linear regression of the joint height plotted against $\sin\beta$ (Figure 6(d)). The joint height was determined by subtracting the vertical rise due to the distal link bent at angle γ from the height of the end effector measured relative to ground.

C. Comparison of Sensory Array to IMU

After these two calibration procedures, the combination of the joint sensors and buckling sensor generates sufficient data to estimate the angle of the distal linkage and the vertical position of the end effector relative to the ground. To test the accuracy of the state information from the sensors, we completed a test in which we loaded the upright distal linkage with 5lbs and gradually actuated the Grub to lower the weight in a controlled manner (Figure 7). The motion capture system and IMU both recorded the angle and position of the distal linkage. The joint sensors captured the joint angle, θ, and the buckling sensor captured the base angle, β. These two values were combined to generate the estimated angle and vertical position of the distal linkage. From Figure 7(a), we see that the link angle generated from the strain sensor, IMU, and motion capture are in good agreement. Furthermore, when capturing the z-displacement of the end effector (Figure 7(b)), the sensory array matches better to the motion capture data than the IMU data. We believe that this is a result of the conformal sensory sleeve's ability to capture the more complex states and distributed deformations seen in soft systems. We note that a multi-IMU-based system would yield a more accurate representation of the Grub; however, the addition of more rigid components could be detrimental to the overall performance of the system.

D. S-curve Detection

Under higher loads, the constant curvature assumption of the link is no longer valid. The load at the end effector results in bending moments and shear forces throughout the Grub. Because the active joint is the most compliant portion of the system, the end effector loading causes the bellows to develop a second curvature at the distal end, which we refer

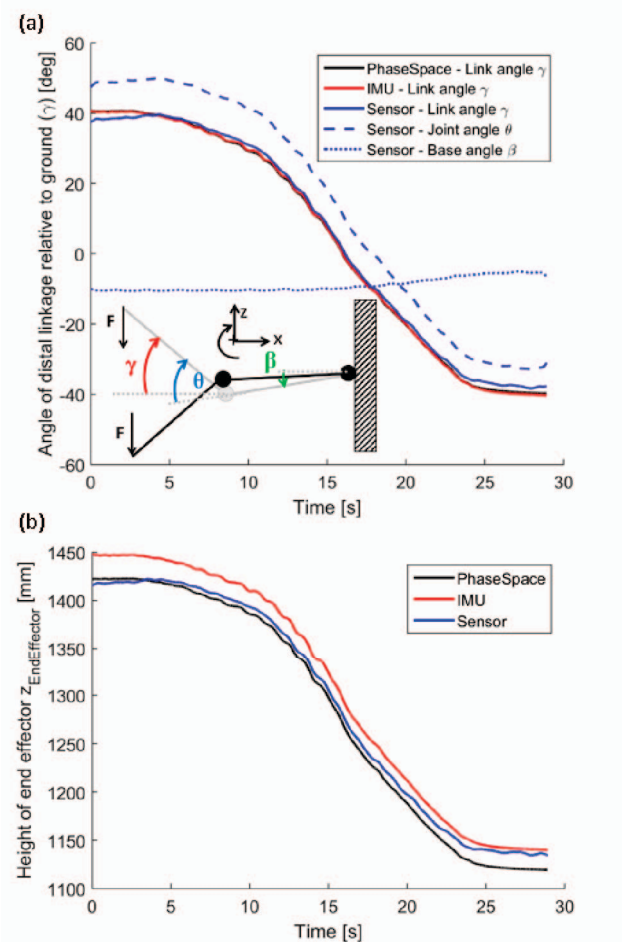

Fig. 7. Comparison between the sensory sleeve, an IMU, and motion capture data to determine joint angle and end effector height. (a) Inset: Experimental procedure where the Grub begins in an upright position and is gradually lowered while holding 5lbs. The plot shows the distal link angle, γ, as measured by the motion capture system, an IMU, and the combination of multiple strain sensor measurements. The sensor link angle, shown in a solid blue line is the sum of the two angles θ and β which were found using the regression equations for the bottom joint sensor and buckling sensor, respectively. (b) Comparison of the height of the end effector as measured by the motion capture system, an IMU and the sensors during the course of the actuation.

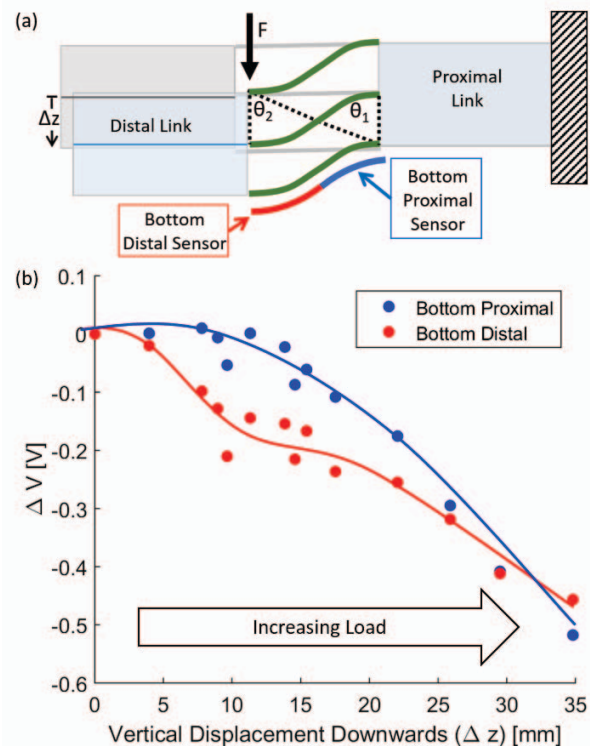

Fig. 8. (a) Diagram of the active joint of the Grub showing the two curvatures comprising the S-curve that appears due to the applied load. The two sensors used in this experiment are located on the bottom side of the joint. (b) Plot of the response of two sensors, as a function of downward vertical displacement that occurs as the end effector of the Grub is loaded while the bellows are inflated to maintain a constant 0° angle between the distal link and the ground.

to as the "S-curve", shown in Figure 8(a). Using two sensors on the bottom of the joint, we were able to detect when this S-curve develops. We collected the data shown in Figure 8(b) by incrementally loading the Grub while simultaneously keeping the proximal and distal links approximately parallel to the ground; this required increasing inflation of the bellows with increasing load. At the start of the test, the Grub is unloaded and the end effector has no vertical displacement (Δz=0). Hence, the sensors are both unstrained and show same response. At relatively low loads (resulting in vertical displacements between 3mm and 25mm in Figure 8(b)), the joint develops the S-curve. Comparing the two sensor responses, the bottom distal sensor has a sharper response, indicating more strain, and thus larger curvature, relative to what the bottom proximal sensor experiences. However, as the Grub is loaded further, the bellows are inflated to higher pressures to maintain the horizontal orientation of the distal link. Therefore, the stiffness of the bellows region increases, which moves the inflection point of the S-curve towards the base until it reaches the junction between the proximal link and the bellows. This causes the compound curvature of the joint to transition towards a single curvature, resulting in the convergence of the sensor responses. In Figure 8(b), this convergence is observed at displacements beyond 25mm. Detection of compound curvatures is crucial for proprioception in continuum or quasi-continuum joints such as the Grub. The results generated here using the dual-sensor design demonstrate the ability of the sensory sleeve to capture complex state information beyond simple joint angle.

VI. Conclusion and Future Work

In this work, we demonstrated the use of a fabric-based capacitive sensing array for state reconstruction of a 1DoF pneumatic arm. The sensing array was composed of high-deformation capacitive strain sensors that were manufactured by screenprinting dielectric silicone elastomers and conductive silicone elastomer composites into Spandex fabric. We then demonstrated that these sensors exhibit a linear change in capacitance due to applied linear strain or curvature. Using a sleeve composed of a single sensor for each side of the pneumatic arm and a buckling sensor, we tracked not only the joint angle of a soft pneumatic arm, but also the vertical

displacement due to buckling in passive linkages. Compared to the performance of a single IMU, the sensor sleeve matched the IMU's accuracy in determining joint angle and outperformed the IMU in determining the vertical position of the end effector. Finally, we demonstrated that a dual-sensor-per-side sleeve can be used to track the compound curvature deformation in the joint of a pneumatic arm.

Future work may be focused in several directions: improvement of the sensor signal conditioning, integrating the sensory sleeve directly into the pneumatic joint, expanding the sensory array, and multimodal sensing. The sensor signal conditioning can be improved by reducing noise, increasing the sensitivity of the sensors to the operating range of strain. Integrating the sleeve directly into the fabric comprising the pneumatic joint would have multiple benefits, including ensuring that the sensors are fixed to the surface of the robot and eliminating slackness of the sensory sleeve. Expansion of the sensory array would increase the resolution of the surface strain mapping of the pneumatic manipulator. However, this must be balanced with the increased number of interface electronics. While the sensors developed in this work were solely used for surface strain measurement, capacitive sensors have been used for pressure and contact sensing. Integration of these sensing modes alongside the strain sensors would result in a data-rich soft sensing system. Further progress in sensory skins and fabrics will enable accurate state estimation, and therefore closed-loop control of soft systems without the limiting confines of visual feedback.

VII. Acknowledgments

This work was supported by a Robotics Fast Track program (GS-10F0-247U) from the Defense Advanced Research Projects Agency. The Grub utilized for testing was designed and built under an Otherlab NASA SBIR Phase 1 Contract (NNX14CA56P). MCY and ELW are supported by the National Science Foundation Graduate Research Fellowship (Grant DGE-1333468). Any opinion, findings, and conclusions or recommendations expressed in this material are those of the authors and do not necessarily reflect the views of the Defense Advanced Research Projects Agency, National Aeronautics and Space Administration or the National Science Foundation.

References

[1] N. Hogan, "Impedance Control: An Approach to Manipulation: Part III Applications," *J. Dyn. Sys., Meas., Control*, vol. 107, no. 1, pp. 17–24, Mar. 1985.

[2] D. Rus and M. T. Tolley, "Design, fabrication and control of soft robots," *Nature*, vol. 521, no. 7553, pp. 467–475, May 2015.

[3] F. Daerden and D. Lefeber, "Pneumatic artificial muscles: actuators for robotics and automation," *European journal of mechanical and environmental engineering*, vol. 47, no. 1, pp. 11–21, 2002.

[4] Y. L. Park, B. r. Chen, and R. J. Wood, "Soft artificial skin with multimodal sensing capability using embedded liquid conductors," in *2011 IEEE Sensors*, Oct. 2011, pp. 81–84.

[5] Y.-L. Park, B.-R. Chen, and R. J. Wood, "Design and Fabrication of Soft Artificial Skin Using Embedded Microchannels and Liquid Conductors," *IEEE Sensors Journal*, vol. 12, no. 8, pp. 2711–2718, Aug. 2012.

[6] E. L. White, J. C. Case, and R. K. Kramer, "Multi-Element Strain Gauge Modules for Soft Sensory Skins," *IEEE Sensors Journal*, vol. 16, no. 8, pp. 2607–2616, Apr. 2016.

[7] A. Tognetti, F. Lorussi, R. Bartalesi, S. Quaglini, M. Tesconi, G. Zupone, and D. De Rossi, "Wearable kinesthetic system for capturing and classifying upper limb gesture in post-stroke rehabilitation," *Journal of NeuroEngineering and Rehabilitation*, vol. 2, no. 1, p. 1, 2005.

[8] D. J. Lipomi, M. Vosgueritchian, B. C.-K. Tee, S. L. Hellstrom, J. A. Lee, C. H. Fox, and Z. Bao, "Skin-like pressure and strain sensors based on transparent elastic films of carbon nanotubes," *Nature Nanotechnology*, vol. 6, no. 12, pp. 788–792, Oct. 2011.

[9] W. Hu, X. Niu, R. Zhao, and Q. Pei, "Elastomeric transparent capacitive sensors based on an interpenetrating composite of silver nanowires and polyurethane," *Applied Physics Letters*, vol. 102, no. 8, p. 083303, Feb. 2013.

[10] W. Zeng, L. Shu, Q. Li, S. Chen, F. Wang, and X.-M. Tao, "Fiber-Based Wearable Electronics: A Review of Materials, Fabrication, Devices, and Applications," *Adv. Mater.*, vol. 26, no. 31, pp. 5310–5336, Aug. 2014.

[11] O. Atalay, W. Kennon, and E. Demirok, "Weft-Knitted Strain Sensor for Monitoring Respiratory Rate and Its Electro-mechanical Modelling," *IEEE Sensors Journal*, vol. Early Access Online, 2014.

[12] C. Merritt, H. Nagle, and E. Grant, "Textile-Based Capacitive Sensors for Respiration Monitoring," *IEEE Sensors Journal*, vol. 9, no. 1, pp. 71–78, Jan. 2009.

[13] D. P. Cotton, I. M. Graz, and S. P. Lacour, "A multifunctional capacitive sensor for stretchable electronic skins," *IEEE Sensors Journal*, vol. 9, no. 12, pp. 2008–2009, 2009.

[14] L. Cai, L. Song, P. Luan, Q. Zhang, N. Zhang, Q. Gao, D. Zhao, X. Zhang, M. Tu, F. Yang, W. Zhou, Q. Fan, J. Luo, W. Zhou, P. M. Ajayan, and S. Xie, "Super-stretchable, Transparent Carbon Nanotube-Based Capacitive Strain Sensors for Human Motion Detection," *Scientific Reports*, vol. 3, Oct. 2013.

[15] D. J. Cohen, D. Mitra, K. Peterson, and M. M. Maharbiz, "A Highly Elastic, Capacitive Strain Gauge Based on Percolating Nanotube Networks," *Nano Letters*, vol. 12, no. 4, pp. 1821–1825, Apr. 2012.

[16] B. O'Brien, T. Gisby, and I. A. Anderson, "Stretch sensors for human body motion," vol. 9056, 2014, pp. 905 618–905 618–9.

[17] D. Xu, T. A. Gisby, S. Xie, and I. A. Anderson, "Scalable sensing electronics towards a motion capture suit," Y. Bar-Cohen, Ed., Apr. 2013, p. 86872L.

[18] S. Yao and Y. Zhu, "Wearable multifunctional sensors using printed stretchable conductors made of silver nanowires," *Nanoscale*, vol. 6, no. 4, pp. 2345–2352, 2014.

[19] C. M. Best, J. P. Wilson, and M. D. Killpack, "Control of a pneumatically actuated, fully inflatable, fabric-based, humanoid robot," in *2015 IEEE-RAS 15th International Conference on Humanoid Robots (Humanoids)*, Nov. 2015, pp. 1133–1140.

[20] M. T. Gillespie, C. M. Best, and M. D. Killpack, "Simultaneous position and stiffness control for an inflatable soft robot," in *2016 IEEE International Conference on Robotics and Automation (ICRA)*, May 2016, pp. 1095–1101.

[21] O. J. Woodman, "An introduction to inertial navigation," *University of Cambridge, Computer Laboratory, Tech. Rep. UCAMCL-TR-696*, vol. 14, p. 15, 2007.

[22] A. D. Marchese, K. Komorowski, C. D. Onal, and D. Rus, "Design and control of a soft and continuously deformable 2d robotic manipulation system," in *2014 IEEE International Conference on Robotics and Automation (ICRA)*. IEEE, 2014, pp. 2189–2196.

[23] H. Wang, W. Chen, X. Yu, T. Deng, X. Wang, and R. Pfeifer, "Visual servo control of cable-driven soft robotic manipulator," in *2013 IEEE/RSJ International Conference on Intelligent Robots and Systems*. IEEE, 2013, pp. 57–62.

[24] Y.-L. Park and R. J. Wood, "Smart pneumatic artificial muscle actuator with embedded microfluidic sensing," in *SENSORS, 2013 IEEE*. IEEE, 2013, pp. 1–4.

[25] Y.-L. Park, B.-r. Chen, C. Majidi, R. J. Wood, R. Nagpal, and E. Goldfield, "Active modular elastomer sleeve for soft wearable assistance robots," in *2012 IEEE/RSJ International Conference on Intelligent Robots and Systems*. IEEE, 2012, pp. 1595–1602.

[26] N. Farrow and N. Correll, "A soft pneumatic actuator that can sense grasp and touch," in *2015 IEEE/RSJ International Conference on Intelligent Robots and Systems (IROS)*, Sept. 2015, pp. 2317–2323.

[27] R. A. Bilodeau, E. L. White, and R. K. Kramer, "Monolithic fabrication of sensors and actuators in a soft robotic gripper," in *Intelligent Robots and Systems (IROS), 2015 IEEE/RSJ International Conference on*. IEEE, 2015, pp. 2324–2329.

[28] R. K. Kramer, C. Majidi, R. Sahai, and R. J. Wood, "Soft curvature sensors for joint angle proprioception," in *2011 IEEE/RSJ International Conference on Intelligent Robots and Systems*. IEEE, 2011, pp. 1919–1926.